

All-fiber microendoscopic polarization sensing at single-photon level aided by deep-learning

MARTIN BIELAK^{1, +}, DOMINIK VAŠINKA^{1, +}, AND MIROSLAV JEŽEK^{1, *}

¹Department of Optics, Faculty of Science, Palacký University, 17. listopadu 1192/12, 77900 Olomouc, Czechia

⁺ These authors contributed equally to this work

^{*} jezek@optics.upol.cz

Compiled August 29, 2024

The polarization of light conveys crucial information about the spatial ordering and optical properties of a specimen. However, precise polarization measurement in challenging conditions, including constrained spaces, low light levels, and high-speed scenarios, remains a severe challenge. Addressing this problem, we introduce a real-time polarization measurement method that is accurate down to a single-photon level and provides complete information about the polarization state. Free of moving components, the polarization sensor utilizes a few-mode fiber followed by a fiber array and a detector array. The calibration of the sensor relies on a neural network yielding unprecedented accuracy across all polarization states, including partially polarized light. We validate the approach by visualizing the polarization structure of biological specimens and the birefringent USAF test. Our method offers an efficient and reliable solution for real-time polarization sensing and microendoscopy under low-light conditions.

1. INTRODUCTION

From ellipsometry to optical communications, from microscopy to sensing, light polarization represents a fundamental element across various scientific disciplines. In particular, the polarization of light emitted by an optically anisotropic specimen carries essential information about its material structure and optical properties. Consequently, conducting a thorough analysis of such specimens demands precise characterization of the emitted light polarization. While relatively straightforward in a controlled environment, accurate polarization measurement under challenging conditions remains a significant obstacle.

Low light intensities, representing the first challenging condition, come with a reduced signal-to-noise ratio, which complicates extracting meaningful polarization information from data burdened with environmental and shot noise. Similarly, conducting high-speed measurements, as the second condition, is accompanied by low signal levels within the acquisition time. While increasing the incident light intensity can help, it is limited by our ability to deliver the optical power to the particular sensing area and, most ultimately, by the photodamage threshold of

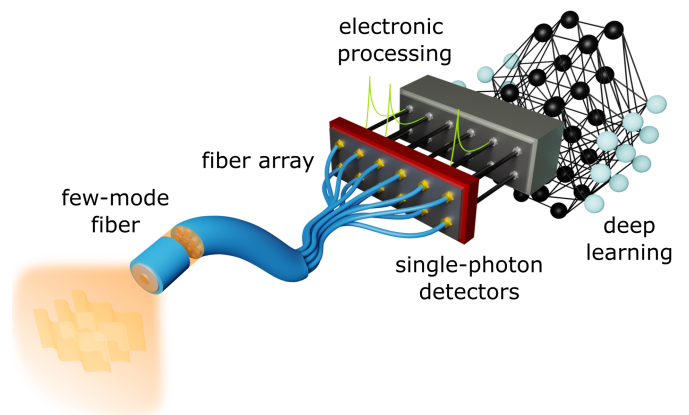


Fig. 1. A visual representation of the all-fiber polarization sensor. Polarized light emitted from a specimen is collected by a short piece of a few-mode fiber. The intermodal interference generates a granular speckle pattern at the output. Several isolated samples of this pattern impinge a fiber array and propagate to a corresponding number of single-photon detectors. The recorded detections are electronically processed using deep learning methods to characterize the incident polarization state.

the sample. Incorporating single-photon detectors can substantially improve the accuracy of protocols relying on the number of detected photons for polarization state reconstruction. However, another drawback arises as these detectors are relatively large and cannot be efficiently integrated. This issue becomes particularly problematic when faced with the third condition - constrained space. Such spaces not only impose restrictions on the overall size of the measurement setup but also limit the placement and alignment of optical components. Therefore, these challenging conditions pose a severe setback, especially for measurements during invasive medical procedures, such as microendoscopy, or internal inspections of materials and products. We address these problems by developing a polarization sensor based on light propagation in disordered media.

Coherent light propagating within a disordered medium is subjected to multimode interference, generating a granular speckle pattern. Despite the apparent degrading effect, the pattern retains encoded information about the incident light [1–4].

Analyzing the light propagation in disordered media and employing suitable post-processing techniques, one can study the disordering effects of the media [5, 6], estimate and classify input images [7–12], learn to modulate the input for projecting a targeted image on the output [13], reconstruct shapes of propagated ultrashort laser pulses [14, 15], compute and communicate [16–20], and even make an accurate spectrometer or wavemeter [21, 22]. Recently, the speckle pattern has proved to preserve a great deal of information about the polarization state of the incident light [23, 24]. Although additional studies successfully advancing the application of disordered-media propagation have been conducted [25–28], developing a compact polarimeter capable of rapid measurements with single-photon sensitivity continues to be an open problem.

Here, we introduce a highly accurate single-shot all-fiber polarization sensor based on intermodal interference in a very short piece of a few-mode fiber. Instead of processing the complete spatial speckle pattern, our approach relies on its sparse sampling in a few isolated points using a fiber array. Fiber-coupled single-photon detectors then allow for high sensitivity down to a single-photon level. The all-fiber sensor contains no moving components or complex metastructures and is sufficiently small for endoscopic procedures. Furthermore, the method can accurately operate at a high repetition rate, processing several thousands of polarization states per second. The setup is aided by a deep machine-learning model reconstructing complete polarization information in real time. The calibrated sensor maintains unparalleled accuracy and stability throughout an extensive period, even for partially-polarized light. We demonstrate the sensing abilities of our approach in polarized light scans of dense connective tissue, moving diatom, and the birefringent USAF test. Our polarization sensor opens new frontiers in precise polarization measurements, providing an indispensable tool for cutting-edge applications in biomedicine, material research, and beyond.

2. EXPERIMENTAL AND DATA PROCESSING SETUP

The speckle-based polarization sensor depicted in Fig. 1 employs a common few-mode fiber to characterize the input polarization state. The sensor collects light with a front face of a 5 cm long step-index SMF28 fiber with a numerical aperture of 0.14 and a core diameter of $8.2 \mu\text{m}$. While the motivation behind choosing this specific fiber type is to minimize the sensing area and keep the speckle structures large, we emphasize that this preference is optional. Virtually any few-mode or multimode fiber, including significantly shorter variants, can be used as a substitute. The main requirement for the fiber is to support several interfering modes necessary for creating a polarization-dependent speckle pattern at the output. Following a 5mm free-space propagation, we collect discrete samples of this interference pattern using a fiber array comprising seven gradient multimode fibers, each with a $62.5 \mu\text{m}$ core diameter, forming a $375 \mu\text{m}$ diameter honeycomb pattern. Each fiber then propagates the collected intensity signal to an independent single-photon avalanche diode, recording the number of detection events. After normalizing the measured counts, this setup associates the sampled polarization state with the corresponding relative frequencies of each detector, which we term a count distribution. For more experimental details, see Sec. S1 in Supplement 1.

Using the sensor, we analyzed 30,000 polarization states, uniformly covering the entire surface of the Poincaré sphere [3]. Our state preparation involved a continuous laser beam with a

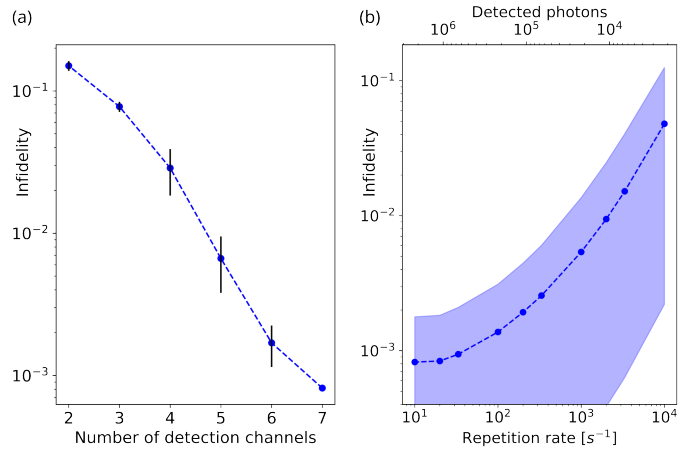


Fig. 2. (a) Polarization error quantified by infidelity for varying numbers of active detectors. Variability bars represent uncertainties arising from different subset combinations. The achieved infidelities underscore the sufficiency of sparse sampling of the speckle pattern. (b) The relation between polarization infidelity, the collective number of detected photons across all detectors, and the measurement repetition rate. The colored area indicates the confidence interval of the test set.

central wavelength of $0.8 \mu\text{m}$ attenuated to the single-photon level and propagated through a linear polarizer. Subsequently, a twisted nematic liquid crystal device [1], controlled by voltage signals, performed a targeted unitary transformation of the polarization state on this weak coherent light. The device operation underwent calibration through bidirectional modeling [31], ensuring fast and precise preparation of arbitrary polarization states. Its accuracy was verified using a reference polarimeter based on wave plates. The polarization state preparation using both methods reaches an average fidelity exceeding 0.999, however, the liquid crystal device operates by orders of magnitude faster. Subsequently, our sensor characterized the prepared polarization state, providing the corresponding detection counts. On average, we acquired approximately 150,000 photon detection events per detector within a 50 ms acquisition time window. Moreover, we expand our dataset to include partially polarized light. We can establish a count distribution for a mixture of two orthogonal states by weight-summing their respective distributions. This approach is virtually equivalent to directly measuring the corresponding mixed state. Employing this method, we assembled an extensive dataset of polarization states distributed uniformly throughout the entire volume of the Poincaré sphere.

We used the dataset to train a fully-connected deep neural network for reconstructing the polarization state given the associated count distribution, see Sec. S1 for details. The optimized and fully-trained network was evaluated on a test set of previously unobserved polarization states, also acquired from the experimental setup. We achieved the unprecedented average infidelity of 8×10^{-4} with a $[5 \times 10^{-5}, 2 \times 10^{-3}]$ confidence interval using the 10th and 90th percentile. These results reflect the highest achievable measurement accuracy as they approach the fidelity of our polarization state preparation. Furthermore, we conducted additional validation of our results using a 1951 USAF test, as detailed in Sec. S2 of Supplement 1. This supplemental analysis provides further insight into the overall performance of our approach.

3. PERFORMANCE EVALUATION

We highlight that our approach eliminates the need for capturing an image of the complete speckle pattern. Instead, we collect a limited number of isolated samples, which are then propagated through the fiber array channels. This substantial reduction in data collection allows for sensitive measurements at extremely low intensities using single-photon detectors. To assess the sensitivity of our approach to the processed portion of the speckle pattern, we investigate the achievable infidelity with regard to the number of employed detection channels. Following the same procedure, we trained additional networks utilizing only a subset of the detection channels as inputs. The infidelities achieved by these networks on corresponding test sets are depicted in Fig. 2 (a). The values represent the averaged errors across multiple trained networks, each employing a distinct combination of detection channel subsets. The results illustrated in this graph unequivocally demonstrate that extracting only a few samples from the speckle pattern provides sufficient information about the polarization state.

We also explored the dependence of the polarization sensing accuracy on the measurement repetition rate, i.e., the inverse value of the acquisition time, representing the number of polarization states characterized per second. Fig. 2 (b) displays the polarization infidelities of a single network, using all seven channels, evaluated for numerous repetition rates. Notably, achieving an average fidelity of 0.999 at a 33 Hz rate holds particular significance. This frequency aligns closely with the borderline on a perceptible frame rate of the human eye. Hence, it underscores the ability of the sensor to operate in real-time sensing applications with high accuracy. Furthermore, our setup demonstrates the capacity to measure over 2,000 polarization states per second while maintaining an average fidelity surpassing 0.99. It is crucial to emphasize that these performances depend on the number of detected photons rather than the repetition rate alone. Consequently, even significantly higher repetition rates can attain the same fidelities with appropriately increased light intensity limited virtually only by saturation of employed single-photon detectors. This feature proves especially beneficial for applications requiring high-repetition-rate sensing.

Furthermore, let us discuss the long-term stability of our approach and its resistance to environmental effects. Despite using a 5cm long few-mode fiber in an open environment without elaborated fixation, the polarization sensor shows sufficient stability for a week without additional calibration or network retraining. For in-situ and microendoscopic applications, the fiber is typically inserted in a cannula, preventing bending and micro deformations. The stability can be further enhanced using a few-mm or sub-mm long fiber encased within a ceramic or glass ferrule tip. The millimeter-long fiber provides sufficient intermodal coupling, and the encasing fixes the fiber and its position relative to the fiber array. With these modifications, we expect an improvement in stability by up to two orders of magnitude. In summary, our polarization sensor represents an outstanding instrument for efficient and accurate real-time and high-speed polarimetry applications.

We first demonstrate the sensing ability of our approach by conducting a polarization-sensitive scan of dense connective tissue (AmScope PS25W). While the primary application of our sensor significantly differs from polarization imaging, this optically anisotropic specimen is famously known in the polarization microscopy field. Visualizing its typical structures further underscores the accuracy of the presented polarimet-

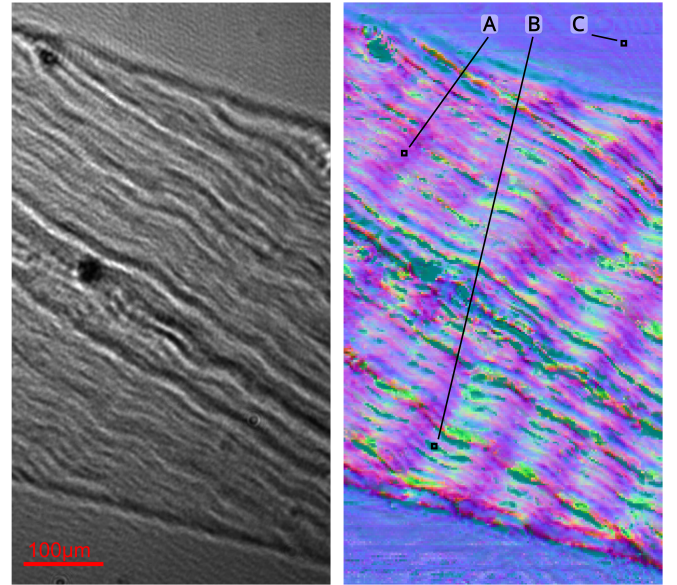


Fig. 3. Visualization of dense connective tissue: (left) intensity image and (right) a scan using the all-fiber polarization sensor. The resulting Bloch parameters are represented as an RGB false-colored image. The three highlighted pixels characterize the purple and green segments in the polarization structure alongside a reference background polarization. Their respective Bloch parameters are $A = (0.34, -0.43, 0.82)$, $B = (-0.90, 0.05, 0.06)$, and $C = (-0.04, -0.18, 0.98)$.

ric sensor. Using the experimental arrangement outlined in Sec. 2 and Supplement 1 Sec. S1, we replaced the calibration polarization preparation stage with the tissue specimen. The few-mode fiber positioned proximal to the tissue scanned over its area, capturing the induced polarization transformation. The reconstructed polarization states were expressed as three Bloch parameters, i.e., renormalized Stokes parameters [3], and visualized as a false-colored RGB image. In Fig. 3, we present a side-by-side comparison of this polarization scan with an intensity image captured from an identical tissue region. This intensity image was obtained using a monochrome camera (ImagingSource DMK 23U274) with a pixel size of $4.4 \times 4.4 \mu\text{m}$. We illuminated the specimen with $0.8 \mu\text{m}$ light and projected the resulting image onto the camera through a 25.4 mm focal-length lens, providing an estimated fivefold magnification. As illustrated in Fig. 3, the polarization sensor reveals underlying polarization structures that remain concealed in the intensity profile. Refer to Fig. S3 of Supplement 1 for a comparison with the corresponding image acquired using a stand-alone polarization microscope.

As the dense connective tissue is a static specimen, the previous polarization scan can be acquired using advanced imaging polarimeters based on rotating waveplates and a CCD/CMOS camera. However, a polarization measurement using wave plates is an insufficient method for characterizing a rapidly changing polarization state induced by moving or evolving specimens. These scenarios require significantly faster approaches that can be performed in a single-shot regime. We demonstrate the feasibility of our sensor for such applications by conducting a polarization measurement to characterize the floating diatom. These microscopic unicellular organisms comprise a complex inner structure that can exhibit anisotropic properties. By continuously measuring the polarization state, we characterized the

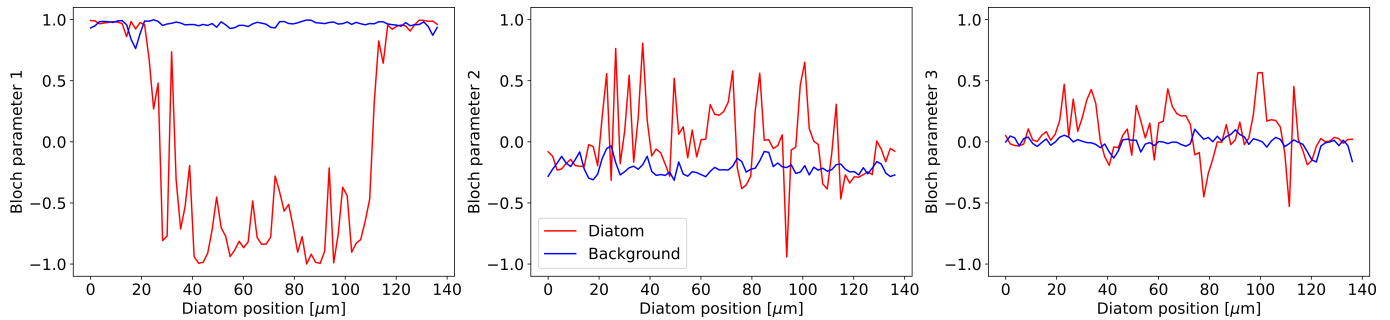


Fig. 4. A time evolution of a polarization state measured by the polarimetric all-fiber sensor and characterized using three Bloch parameters. The red color corresponds to changes induced by an anisotropic diatom passing in front of the fiber tip. For comparison, the blue line represents the same environment without diatoms. The modulation visible in all three Bloch parameters indicates the properties of a polarization-affecting element moving in front of the sensor, allowing further study of the specimen.

polarization transition caused by a moving diatom within the same experimental arrangement as in the previous application. The evolution of the Bloch parameters corresponding to this dynamic process is depicted in Fig. 4 with red lines. Compared to the blue lines of background polarization, the diatom properties are visible in the modulation of Bloch parameters. One could count the number of living specimens, estimate their size and shape, or even classify the detected organisms based on their birefringent properties. The sensor can also find applications for in-situ material inspection, local strain analysis, and micro crystal growth monitoring. These showcases underscore the versatility of our polarization sensor for various sensing applications and its valuable contributions to low-light high-speed polarimetry.

4. CONCLUSION

We have developed a single-shot polarization sensor based on light propagation through a short piece of a few-mode fiber, resulting in a polarization-dependent speckle pattern. The defining aspect of our approach is the sparse sampling of this pattern using a fiber array instead of capturing the whole intensity profile. This characteristic allows the use of any photonic detectors, including high-speed or single-photon detectors, enabling fast response and operation at low light intensities. The implementation of deep learning algorithms in the system ensures an accurate reconstruction, providing complete information about the polarization state, including partial polarization, with an infidelity of 8×10^{-4} . Complemented by the high operation speed, it allows for both real-time and high-repetition-rate polarization sensing with remarkable precision. The all-fiber sensor, featuring a compact design with no moving components, is particularly well-suited for reducing the invasiveness of biomedical procedures in constrained spaces and under low-light conditions. Furthermore, we can enhance the spatial resolution of our sensor by tapering the tip of the few-mode fiber. This method could even provide comparable resolution as near-field scanning optical microscopy while preserving the single-photon polarization sensitivity. In the view of optically-assisted machine learning, the random propagation in multimode fiber followed by a computational neural network represents an instance of an extreme learning machine or reservoir computing [19, 32]. By demonstrating the single-photon sensing capability of these architectures, we have provided the foundation for decreasing energy consumption in optical sensing and computing. In summary, our polarization sensor significantly advances the field, offering

a combination of compactness, accuracy, low light sensitivity, and high operational speed that opens up new possibilities for highly accurate polarization sensing across various applications.

Funding. This work was supported by the Czech Science Foundation (project 21-18545S), Ministry of Education, Youth, and Sports of the Czech Republic (project OP JAC CZ.02.01.01/00/23_021/0008790). MB and DV acknowledge the support by Palacký University (projects IGA-PrF-2023-006 and IGA-PrF-2024-008).

Acknowledgments. We acknowledge the use of cluster computing resources provided by the Department of Optics, Palacký University Olomouc. We thank Jan Provazník for maintaining the cluster and providing support. We also thank Josef Hloušek for developing a 3D model shown in Fig. 1 and Jaromír Běhal for a fruitful discussion on birefringent biological samples.

Disclosures. The authors declare no conflicts of interest.

Data Availability Statement. The code and data that support the findings of this study are publicly available on GitHub [33].

REFERENCES

1. S. Rotter and S. Gigan, "Light fields in complex media: Mesoscopic scattering meets wave control," *Rev. Mod. Phys.* **89**, 015005 (2017).
2. J. Bertolotti and O. Katz, "Imaging in complex media," *Nat. Phys.* **18**, 1008–1017 (2022).
3. H. Cao, A. P. Mosk, and S. Rotter, "Shaping the propagation of light in complex media," *Nat. Phys.* **18**, 994–1007 (2022).
4. K. Vynck, R. Pierrat, R. Carminati, L. S. Froufe-Pérez, F. Scheffold, R. Sapienza, S. Vignolini, and J. J. Sáenz, "Light in correlated disordered media," *Rev. Mod. Phys.* **95**, 045003 (2023).
5. E. Valent and Y. Silberberg, "Scatterer recognition via analysis of speckle patterns," *Optica* **5**, 204–207 (2018).
6. M. W. Matthès, Y. Bromberg, J. de Rosny, and S. M. Popoff, "Learning and avoiding disorder in multimode fibers," *Phys. Rev. X* **11**, 021060 (2021).
7. T. Čižmár and K. Dholakia, "Exploiting multimode waveguides for pure fibre-based imaging," *Nat. Commun.* **3**, 1027 (2012).
8. M. Plöschner, T. Tyc, and T. Čižmár, "Seeing through chaos in multimode fibres," *Nat. Photonics* **9**, 529–535 (2015).
9. N. Borhani, E. Kakkava, C. Moser, and D. Psaltis, "Learning to see through multimode fibers," *Optica* **5**, 960–966 (2018).
10. Y. Li, Y. Xue, and L. Tian, "Deep speckle correlation: a deep learning approach toward scalable imaging through scattering media," *Optica* **5**, 1181–1190 (2018).
11. B. Rahmani, D. Loterie, G. Konstantinou, D. Psaltis, and C. Moser, "Multimode optical fiber transmission with a deep learning network," *Light. Sci. & Appl.* **7**, 69 (2018).
12. P. Caramazza, O. Moran, R. Murray-Smith, and D. Faccio, "Transmission of natural scene images through a multimode fibre," *Nat. Commun.* **10**, 2029 (2019).
13. B. Rahmani, D. Loterie, E. Kakkava, N. Borhani, U. Teġin, D. Psaltis, and C. Moser, "Actor neural networks for the robust control of partially measured nonlinear systems showcased for image propagation through diffuse media," *Nat. Mach. Intell.* **2**, 403–410 (2020).
14. R. Ziv, A. Dikopoltsev, T. Zahavy, I. Rubinstein, P. Sidorenko, O. Cohen, and M. Segev, "Deep learning reconstruction of ultrashort pulses from 2d spatial intensity patterns recorded by an all-in-line system in a single-shot," *Opt. Express* **28**, 7528–7538 (2020).
15. W. Xiong, B. Redding, S. Gertler, Y. Bromberg, H. D. Tagare, and H. Cao, "Deep learning of ultrafast pulses with a multimode fiber," *APL Photonics* **5**, 096106 (2020).
16. H. Defienne, M. Barbieri, I. A. Walmsley, B. J. Smith, and S. Gigan, "Two-photon quantum walk in a multimode fiber," *Sci. Adv.* **2**, e1501054 (2016).
17. S. Leedumrongwathanakun, L. Innocenti, H. Defienne, T. Juffmann, A. Ferraro, M. Paternostro, and S. Gigan, "Programmable linear quantum networks with a multimode fibre," *Nat. Photonics* **14**, 139–142 (2020).
18. N. H. Valencia, S. Goel, W. McCutcheon, H. Defienne, and M. Malik, "Unscrambling entanglement through a complex medium," *Nat. Phys.* **16**, 1112–1116 (2020).
19. D. Pierangeli, G. Marcucci, and C. Conti, "Photonic extreme learning machine by free-space optical propagation," *Photonics Res.* **9**, 1446–1454 (2021).
20. B. Courme, P. Cameron, D. Faccio, S. Gigan, and H. Defienne, "Manipulation and certification of high-dimensional entanglement through a scattering medium," *PRX Quantum* **4**, 010308 (2023).
21. B. Redding, S. F. Liew, R. Sarma, and H. Cao, "Compact spectrometer based on a disordered photonic chip," *Nat. Photonics* **7**, 746–751 (2013).
22. R. K. Gupta, G. D. Bruce, S. J. Powis, and K. Dholakia, "Deep learning enabled laser speckle wavemeter with a high dynamic range," *Laser & Photonics Rev.* **14**, 2000120 (2020).
23. M. Juhl and K. Leosson, "Polarimetry with disordered photonic structures," *ACS Photonics* **7**, 203–211 (2020).
24. M. Facchin, G. D. Bruce, and K. Dholakia, "Speckle-based determination of the polarisation state of single and multiple laser beams," *OSA Continuum* **3**, 1302–1313 (2020).
25. N. A. Rubin, P. Chevalier, M. Juhl, M. Tamagnone, R. Chipman, and F. Capasso, "Imaging polarimetry through metasurface polarization gratings," *Opt. Express* **30**, 9389–9412 (2022).
26. D. Pierangeli and C. Conti, "Single-shot polarimetry of vector beams by supervised learning," *Nat. Commun.* **14**, 1831 (2023).
27. M. Stibůrek, P. Ondráčková, T. Tučková, S. Turtaev, M. Šiler, T. Pikálek, P. Jákl, A. Gomes, J. Krejčí, P. Kolbábková, H. Uhlířová, and T. Čižmár, "110 μm thin endo-microscope for deep-brain in vivo observations of neuronal connectivity, activity and blood flow dynamics," *Nat. Commun.* **14**, 1897 (2023).
28. S. Goel, C. Conti, S. Leedumrongwathanakun, and M. Malik, "Referenceless characterization of complex media using physics-informed neural networks," *Opt. Express* **31**, 32824–32839 (2023).
29. S. Huard, *Polarization of Light* (Wiley, 1997).
30. M. Bielak, R. Stárek, V. Krčmarský, M. Mičuda, and M. Ježek, "Accurate polarization preparation and measurement using twisted nematic liquid crystals," *Opt. Express* **29**, 33037–33052 (2021).
31. D. Vašinka, M. Bielak, M. Neset, and M. Ježek, "Bidirectional deep learning of polarization transfer in liquid crystals with application to quantum state preparation," *Phys. Rev. Appl.* **17**, 054042 (2022).
32. P. Mujal, R. Martínez-Peña, J. Nokkala, J. García-Beni, G. L. Giorgi, M. C. Soriano, and R. Zambrini, "Opportunities in quantum reservoir computing and extreme learning machines," *Adv. Quantum Technol.* **4**, 2100027 (2021).
33. D. Vašinka, "Github repository," <https://github.com/VasinkaD/Polarization-Deep-Sense> (2024).

Supplemental Document

1. DETAILED SENSOR DESCRIPTION

A. Experimental setup

In addition to the information provided in the main text, we include a detailed scheme of our all-fiber polarization sensor, illustrated in Fig. S1. This scheme comprises three configurations. In the first configuration, the twisted nematic liquid crystal device [S1] induces polarization transformation on the attenuated coherent signal generated by a fiber-coupled continuous 810 nm semiconductor laser diode (QPhotonics QFLD). We independently verified the accurate operation of the liquid crystal device in the second configuration by replacing it with a reference polarimeter based on rotating wave plates. The third configuration represents the sensor application and comprises the birefringent specimen under investigation. In all cases, the modified signal is collected by the 5 cm long SMF28 few-mode fiber. The number of modes supported by this fiber is characterized in Subsection B.

The generated speckle pattern propagates through a 5 mm free space before reaching the array of seven gradient multimode fibers GIF625. This propagation allows the speckle grain size to match the multimode fiber core. Arranged in a honeycomb structure with a 375 μm diameter, the multimode fibers have a core diameter of 62.5 μm and a cladding diameter of 125 μm . Each fiber sparsely samples the intensity from the speckle pattern and forwards the signal to an independent single-photon avalanche diode (Excelitas SPCM). The entire experimental setup is located in an unsealed open space of a temperature-maintained laboratory.

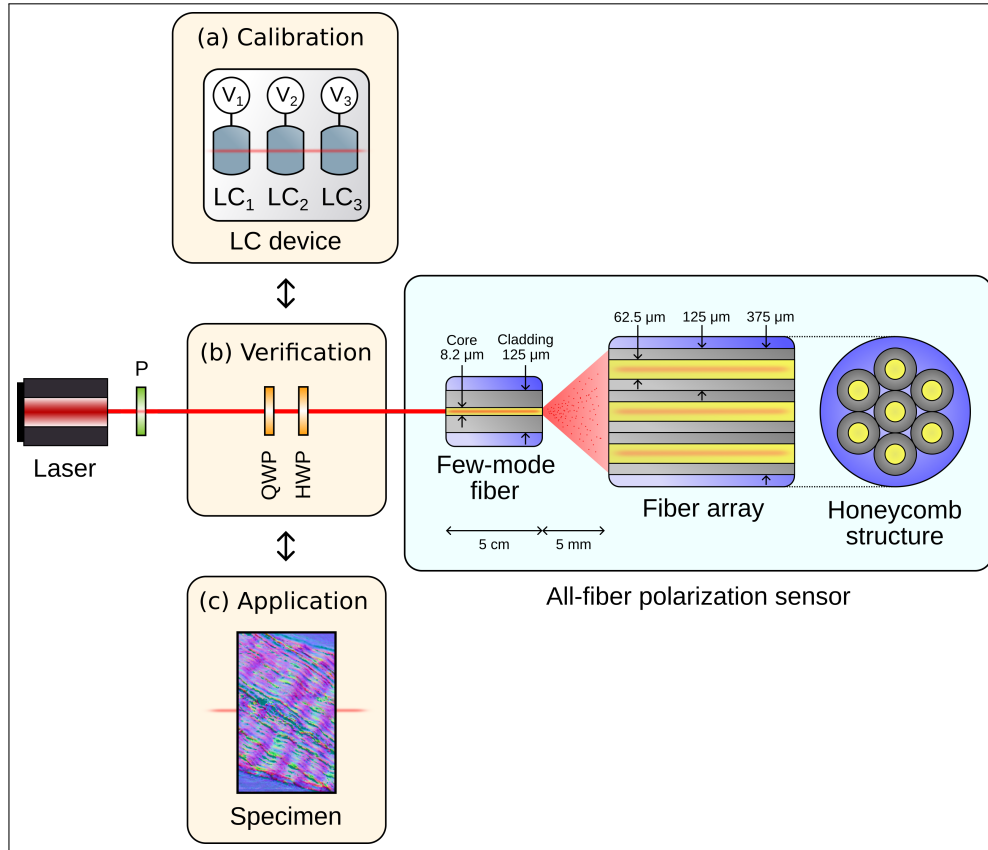


Fig. S1. A detailed visualization of the experimental setup for the all-fiber sensor. The twisted nematic liquid crystal device, labeled as (a), is present only during dataset acquisition for deep neural network training. In the verification stage, depicted in (b), a reference polarimeter based on wave plates is employed to validate the accurate operation of the liquid crystal device. Finally, this segment is replaced with a polarization-modulating specimen (c) during the USAF test, dense connective tissue, and diatom measurements.

B. Supported fiber modes analysis

Determining the exact number of modes M supported by the SMF28 few-mode fiber at the given wavelength proves intricate. Most mathematical formulas are precise only in the limit case of a high mode number. Nevertheless, we estimated M by evaluating the normalized frequency parameter V ,

$$V = \frac{2\pi}{\lambda} r_{\text{core}} \text{NA}, \quad (\text{S1})$$

where $\lambda = 810 \text{ nm}$ is the wavelength of propagated light, $r_{\text{core}} = 4.1 \mu\text{m}$ is the fiber core radius, and $\text{NA} = 0.14$ is the numerical aperture. The calculated value of $V = 4.45 > 2.405$ indicates that the fiber supports more than one mode per polarization direction.

Subsequently, the number of modes M is approximately given by the relation

$$M \approx \frac{V^2}{2} = 9.9, \quad (\text{S2})$$

valid under the assumption that V is large. Since this condition was not fully satisfied, we have also utilized publicly available software developed for mode computation in multimode fibers [S2] and obtained the number of modes $M = 8$.

C. Numerical setup

The physical setup described above is assisted by a numerical processing comprising a deep neural network model. This trained network, consisting of 250 neurons per 4 hidden layers, performs a nonlinear transformation on the count distribution and returns four real-valued outputs. These represent elements of a two-by-two triangular matrix τ with real-valued diagonal entries and a single complex off-diagonal entry. Utilizing the Cholesky decomposition, we can reconstruct a Hermitian positive-definitive matrix $\tau\tau^\dagger$. Upon normalizing its trace to unity, $\rho = \frac{\tau\tau^\dagger}{\text{Tr}[\tau\tau^\dagger]}$ represents a physically sound coherence matrix of the polarization state [S3], mathematically equivalent to a density matrix of a two-level quantum system. Therefore, the complete model can be interpreted as providing the polarization coherence matrix of the collected light given the measured count distribution.

We trained the network using the Adam optimizer and a mean squared error loss function. Various hyperparameters, including network architecture, were fine-tuned to optimize the network performance. For this purpose, we employed a validation set, separated from the training data, to find the optimal hyperparameter combination with respect to a fidelity metric

$$F = \text{Tr} \left[\sqrt{\sqrt{\rho} \cdot \sigma \cdot \sqrt{\rho}} \right]^2 \in [0, 1], \quad (\text{S3})$$

where ρ is the polarization coherence matrix provided by the network and σ is the ground truth matrix of the input polarization state. This metric, which quantifies the closeness between the states, can be expressed in terms of error as infidelity $1 - F$. Finally, the separated experimentally acquired test set was used for the performance evaluation of the optimal network.

2. 1951 USAF BIREFRINGENT TEST

We performed an additional analysis beyond those presented in the main text. Specifically, we conducted a scan of a 1951 USAF birefringent resolution test with the developed polarization sensor and compared it with a polarization measurement based on rotating wave plates. Fig. S2 shows a polarization image obtained with the standard method (a) alongside the scan using our all-fiber sensor (b). Both panels visualize false-colored RGB images using Bloch parameters (B_1, B_2, B_3) with $R = \frac{B_1+1}{2}$, $G = \frac{B_2+1}{2}$, and $B = \frac{B_3+1}{2}$ corresponding to red, green, and blue channel intensities. By averaging over the background and polarization-modulating regions, we estimated a fidelity value of approximately 0.986 between the two polarization measurement approaches. This comparison unequivocally demonstrated the ability of our sensor to perform highly accurate polarization measurements.

Additionally, the image shown in panel (b) allows for the evaluation of the spatial resolution of our sensor. To this end, we fitted horizontally and vertically oriented edges at several positions. Characterized as the 20% to 80% width, we estimated the resolution to be approximately $(6 \pm 5) \mu\text{m}$. Besides the distance from a specimen to the fiber tip, the resolution is dictated by the few-mode fiber diameter and can be modified by employing different fiber types. Moreover, tapering the fiber tip could improve the resolution of our sensor up to the near-field scanning optical microscopy level.

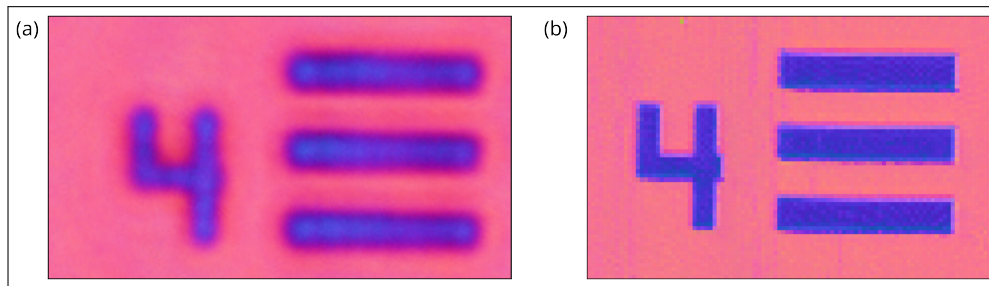


Fig. S2. A comparison of polarization measurement on a region of the 1951 USAF birefringent resolution test. (a) A polarization image obtained using standard imaging based on rotating wave plates. (b) An all-fiber sensor scan of the same region. Both results are visualized as false-colored RGB images using Bloch parameters.

3. DENSE CONNECTIVE TISSUE

In the main text, we demonstrated our sensor by performing a polarization scan of dense connective tissue. For comparative purposes, Fig. S3 includes an additional panel depicting a polarization image of the same specimen obtained using a stand-alone polarization microscope. Its experimental setup comprises a monochrome camera (ImagingSource DMK 23U274) and a pair of crossed polarizers. The typical inner structure of the dense connective tissue is evident in both polarization images, confirming that our sensor indeed performs polarization characterization of this sample. Moreover, the false-color image provided by our sensor contains complete information about the polarization states.

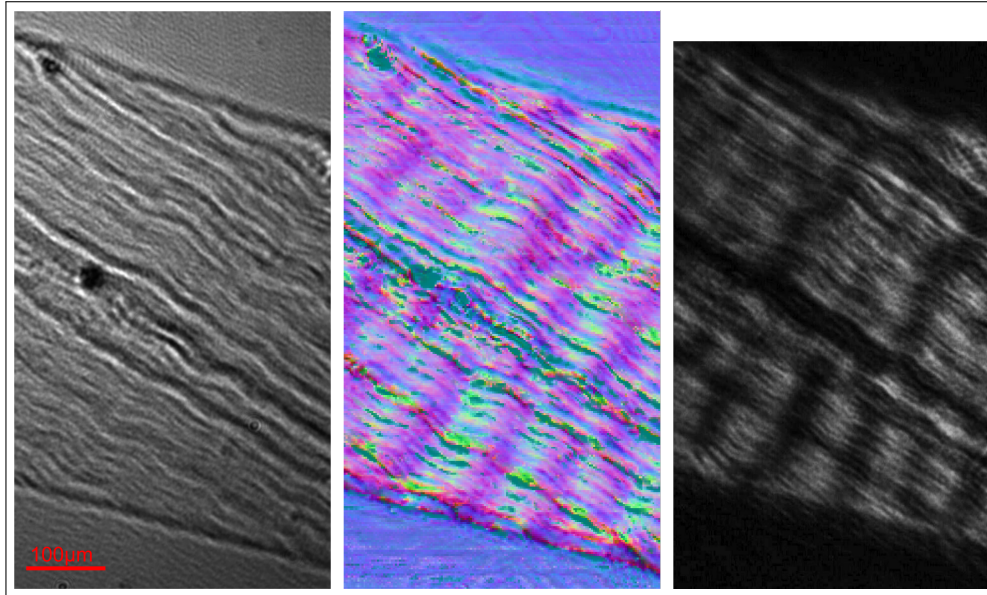


Fig. S3. Visualization of dense connective tissue: (left) an intensity image, (middle) a scan using the all-fiber polarization sensor, (right) an image using a stand-alone polarization microscope. The first two panels reproduce results from the main text. The additional panel quantitatively verifies the tissue polarization structures via a common crossed-polarizers microscope.

REFERENCES

- [S1] M. Bielak, R. Stárek, V. Krčmarský, M. Mičuda, and M. Ježek, "Accurate polarization preparation and measurement using twisted nematic liquid crystals," *Opt. Express* **29**, 33037–33052 (2021).
- [S2] S. M. Popoff, "Replicate depository," <https://replicate.com/wavefrontshaping/pymmf> (2018).
- [S3] S. Huard, *Polarization of Light* (Wiley, 1997).